Nanoelectronics and Its New Materials – A NEW ERA OF NANOSCIENCE

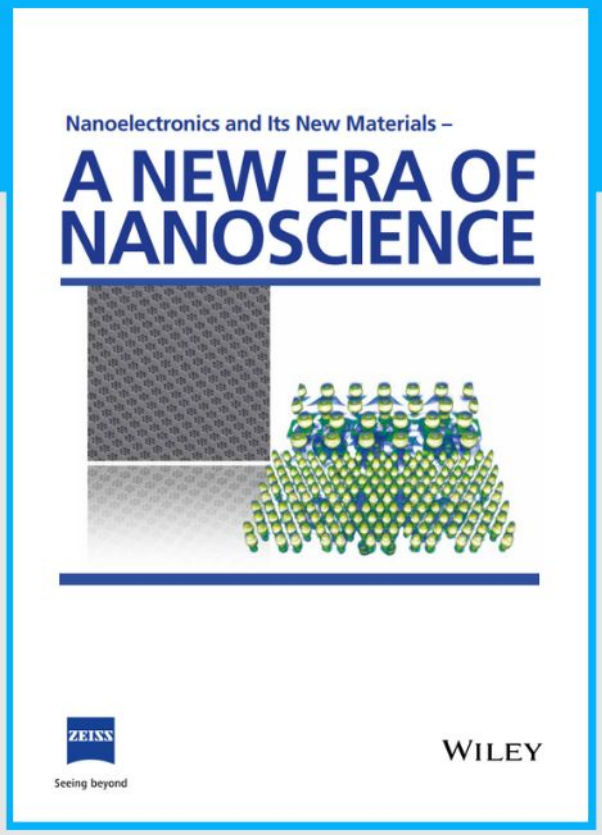

Discover the recent advances in electronics research and fundamental nanoscience.

Nanotechnology has become the driving force behind breakthroughs in engineering, materials science, physics, chemistry, and biological sciences. In this compendium, we delve into a wide range of novel applications that highlight recent advances in electronics research and fundamental nanoscience. From surface analysis and defect detection to tailored optical functionality and transparent nanowire electrodes, this eBook covers key topics that will revolutionize the future of electronics.

To get your hands on this valuable resource and unleash the power of nanotechnology, simply download the eBook now. Stay ahead of the curve and embrace the future of electronics with nanoscience as your guide.

ZEISS

Seeing beyond

WILEY

ADVANCED FUNCTIONAL MATERIALS
www.afm-journal.de

Integrating Metal Complex Units and Redox Sites into Thorium-Based Metal–Organic Frameworks for Selective Photocatalytic Oxidation of Sulfides

Xiu-Fen Li, Pengfei Wu, Liang Kan, Qian Niu, Sheng-Nan Sun, Qing Huang, and Ya-Qian Lan**

A series of high-symmetry Th_6–metal-organic frameworks (MOFs) are constructed using various metal complex units and the thorium (Th) cluster, and then being applied as a well-defined catalyst model in the photocatalytic oxidation of methyl phenyl sulfide reactions. The integration of Th_6-MOFs by incorporating metal complex units and redox sites (Th_6 cluster and single-metal site) can effectively modulate the conversion rate and selectivity. Among them, Ni–PBA–Th_6 (PBA = 4-pyridin-4-yl benzoic acid) achieves up to ≈99% conversion and ≈97% selectivity for methyl phenyl sulfone. Experiments and theoretical calculations further elucidate that Th_6 cluster is the catalytic site for the oxidation of methyl phenyl sulfide to methyl phenyl sulfone, while Ni–PBA is the catalytic site for the reduction of hydrogen peroxide. This work sheds new insight into the structural design and photocatalytic application of more efficient thorium-based MOF catalysts.

1. Introduction

Thorium (Th) element, as one of the most abundant actinides on earth, shows enormous potential applications in the nuclear energy feedstock, medical and industrial fields owing to its nuclear attribute, heat and radiation resistance.[1] Therefore, it is of great necessity to explore the chemical behavior and performance of Th-based materials during these applications. Relative to these metal ions (e.g., Zr^{4+}, Hf^{4+}, and Ce^{4+}),[2] Th usually exists in a similar state (IV) but has a larger ionic radius and more bonding front orbital, which may facilitate the construction of metal node with richer coordination patterns and more diverse linkages, finally giving rise to new types of structures.[3] Metal–organic frameworks (MOFs) are highly tunable due to the inclusion of different inorganic metal nodes and functional organic ligands, making them structurally diverse.[4] Introducing Th or its clusters into MOF structures not only helps to study the chemical behavior of Th,[5] but allows the construction of new Th-MOFs with unique chemical and physical properties.[6] These characters have many potential applications in various aspects, such as gas separation,[7] heterogeneous catalysis,[8] and radiation detection.[9] However, fundamental properties including thermodynamics, electronics, or detailed photophysics are currently lacked in the field of Th-MOFs, and the field of Th-based materials for photo/thermal catalysis applications is yet to be explored.[10] Furthermore, Th^{4+} is strongly Lewis acidic and its hydrolysis is very rapid, leading to the coexistence of multimers (e.g., dimers, tetramers, hexamers, octamers, or decamers). This makes it difficult for Th to form a fixed framework structure.[11] The synthetic challenges of Th-MOF materials have limited their research in various catalytic fields. Only a few Th-MOFs have been reported for CO_2 cycloaddition,[8b] benzylamine oxidative coupling,[12] etc. However, Th-MOFs, as a novel heterogeneous molecular catalyst with a precise crystal structure, defined catalytic active center, and evenly distributed active site, are expected to improve the conversion and selectivity of catalytic reaction. The precise structure of MOFs also provides a visualization platform that can clearly reveal the catalytic mechanism and chemical activity of Th element. Therefore, it is necessary to develop more Th-MOF catalysts to explore more catalytic applications and mechanisms of Th element.

Sulfur oxides (SO_x) generated from the combustion of sulfides in fuels are a significant contributor of air pollution, causing acid rain and particulate matter.[13] One potential solution for reducing the sulfur content of fuels and mitigating its impact on the environment and the energy industry is to oxidize them to sulfoxide and sulfone, in addition to separating SO_x from combustion products through selective trapping.[14] Furthermore, methyl phenyl sulfone ($MPSO_2$) is one of the very important organic compounds,[15] and sulfone derivativeshave a wide range of applications in pesticides, pharmaceuticals, and food flavors.[16]

X.-F. Li, L. Kan, S.-N. Sun, Q. Huang, Y.-Q. Lan
School of Chemistry
South China Normal University
Guangzhou 510006, P. R. China
E-mail: huangqing@njfu.edu.cn; yqlan@m.scnu.edu.cn
P. Wu, Q. Huang
College of Materials Science and Engineering Nanjing Forestry University
Nanjing 210037, P. R. China
Q. Niu
School of Chemistry and Materials Science Nanjing Normal University
Nanjing 210023, P. R. China

The ORCID identification number(s) for the author(s) of this article can be found under https://doi.org/10.1002/adfm.202308534

DOI: 10.1002/adfm.202308534

Conventional oxidants or homogeneous catalysts often lead to side reactions with easily oxidized substrates, making it difficult to remove unreacted oxidants, by-products, and catalyst residues from the reaction system.[17] Moreover, enhancing the selectivity of $MPSO_2$ in the catalytic oxidation of methyl phenyl sulfide (MPS) poses another great challenge.[18]

The main catalytic processes for MPS oxidation are thermal catalysis, photocatalysis, and photo–thermal catalysis. In contrast to photocatalysis, high energy consumption is required for thermal and photothermal catalytic reactions, while photocatalysis offers several advantages over traditional thermal catalysis. One of the main advantages is that the photons as the driving forces just need milder conditions relative to other two reactions, resulting in less greenhouse gas emissions and cost-consumption. Another important advantage is that photocatalysis provides opportunities for incompatible redox reactions to occur simultaneously. In addition, photocatalysts can exhibit high catalytic activity and ideal selectivity under light-driving conditions due to efficient charge separation. Efficient photocatalysts require a suitable bandgap width, sufficient oxidation capability, efficient electron–hole separation ability, and a low recombination probability. Most catalysts used for the photocatalytic oxidation of MPS are 2D nanosheets, organic small molecules, and composite materials. The complex structural components limit the mechanistic exploration of the photocatalytic oxidation of MPS. However, MOFs have adjustable structures and functions, and can regulate the bandgap and electron–hole separation ability by assembling different functionalized ligands and metal clusters, promoting the high efficiency of sulfur ether reactions and their catalytic mechanism analysis.[19]

Herein, we have successfully prepared a series of M–L–Th_6 MOF catalysts (M = metal and L = ligand) with similar structures, including Ni–INA–Th_6, Ni—PBA—Th_6, Ni—FCA—Th_6, Ni—MCA—Th_6, Co—INA—Th_6, Co—PBA—Th_6, Co—FCA—Th_6, Co—MCA—Th_6, Cd—INA—Th_6, Cd—PBA—Th_6, Cd—FCA—Th_6, Cd—MCA—Th_6 (INA = isonicotinic acid, PBA = 4-pyridin-4-yl benzoic acid, FCA = 3-fluoroisonicotinic acid, and MCA = 3-methyl-4-pyridinecarboxylic acid). These catalysts feature metal complex units (M—ligands) and Th_6 cluster, which were assembled in M—L—Th_6 MOFs to investigate the performance and mechanism of photocatalytic oxidation of MPS. For the first time, we systematically investigated the effects of metal complex units and Th_6 cluster on the photocatalytic oxidation of MPS, and found that endowing metal complex units and Th_6 cluster in Th_6-MOFs could effectively modulate the conversion rate and selectivity. The series of catalysts were able to convert MPS into both methyl benzyl sulfoxide (MPSO) and $MPSO_2$ products after the photocatalytic reaction. The reaction was significantly accelerated under the light-driven condition compared to the light-free condition, of which Ni—PBA—Th_6 exhibited the most excellent photocatalytic activity with ≈99% conversion rate and ≈97% selectivity for $MPSO_2$. Moreover, Ni—PBA—Th_6 exhibited excellent universality in the photocatalytic oxidation thioether reactions. Experimental characterizations and theoretical calculations indicated that the Th_6 cluster acted as the active site for the oxidation reaction, and the M—ligand acted as the active site for the reduction reaction. To our knowledge, this is a novel approach using thorium-based MOF catalysts for the highly selective oxidation of MPS to $MPSO_2$. It provides a reasonable design strategy for synthesizing the structure of thorium-based MOFs, contributing to their developments and applications.

2. Results and Discussion

A series of M—L—Th_6 MOF crystals (**Figure 1**; Figures S1–S5, Supporting Information) were successfully synthesized using metal complex units (M—ligands) and Th_6 cluster. Single-crystal X-ray diffraction (SC-XRD) analysis revealed that Ni—PBA—Th_6 crystallized in the simple cubic space group *Pm*-3*m* (Tables S1–S3, Supporting Information). The asymmetric unit contained one Th atom (Th1), μ3-O/OH, a hydroxyl molecule, a Ni atom, and a PBA molecule. Th was in the 9-coordinated mode, connecting four μ3-bridged oxygen atoms, four carboxylate oxygen atoms, and one terminal oxygen atom. Six Th(IV) ions bridged to eight μ3-O/OH to form the Th_6O_8 (Th_6 cluster) core, similar to the Zr_6O_8 in UIO-66. Each Th_6 cluster connected outward 12 organic ligands. Ni was in the 6-coordinated mode, linking four PBA ligands and two hydroxyl molecules. The pyridine N atom on the ligand was coordinated to the second metal, forming a M–ligand pattern. Each M—ligand connected four Th_6 cluster through the carboxyl group, resulting into a highly symmetrical 3D structure. The other crystals were isomorphic to Ni—PBA—Th_6, except for differences in the ligand molecules and the second metals used (Figures S6–S9, Supporting Information).

The high purity of the M—ligand—Th_6 samples was confirmed by the comparison of their simulated and synthetic powder XRD (PXRD) patterns (Figures S10–S13, Supporting Information). After 48 h immersion in different organic solvents (*N*, *N*-dimethylformamide (DMF), CH_3OH, C_2H_5OH, CH_3CN, *N*, *N*-dimethylacetamide (DMAc)), the PXRD patterns of M—L—Th_6 MOFs showed that they maintained a stable chemical structure (Figures S14–S19, Supporting Information), indicating they had a good solvent stability, which formed the basis of subsequent catalytic reaction research. The thermogravimetric analysis curves showed that all M—ligand—Th_6 MOFs retained their frameworks below about 300 °C (Figure S20, Supporting Information). X-ray photoelectron spectroscopy (XPS) was performed to confirm the valence states of the thorium and nickel elements. The results indicated only Th (IV) and Ni (II) were present in these MOFs, with binding energies of 344.1 eV ($4f_{5/2}$) and 334.7 eV ($4f_{7/2}$) for Th. 873.1 eV ($2p_{1/2}$) and 855.5 eV ($2p_{3/2}$) for Ni (Figures S21–S23, Supporting Information).

The solid ultraviolet–visible (UV–vis) absorption spectra were used to evaluate the light absorption capacity of these M—L—Th_6 MOFs (Figures S24–S26, Supporting Information). All three M—PBA—Th_6 MOFs with different second metals exhibited a wide range of absorption during the UV region of 200–400 nm, but Ni—PBA—Th_6 had a higher absorbance intensity and also had absorption in the visible region. For Ni—ligand—Th_6 MOFs with different ligands, Ni—PBA—Th_6 exhibited a broader light absorption range (Figure S24, Supporting Information), which indicated its strong light absorption ability and the potential application of photocatalysis. Based on the results of solid UV–vis absorption spectra, the bandgap energy values for Ni—INA—Th_6, Ni—PBA—Th_6, Ni—FCA—Th_6, Ni—MCA—Th_6, Co—INA—Th_6, Co—PBA—Th_6, Co—FCA—Th_6, Co—MCA—Th_6, Cd—INA—Th_6, Cd—PBA—Th_6, Cd—FCA—Th_6, and Cd—MCA—Th_6 were 3.41,

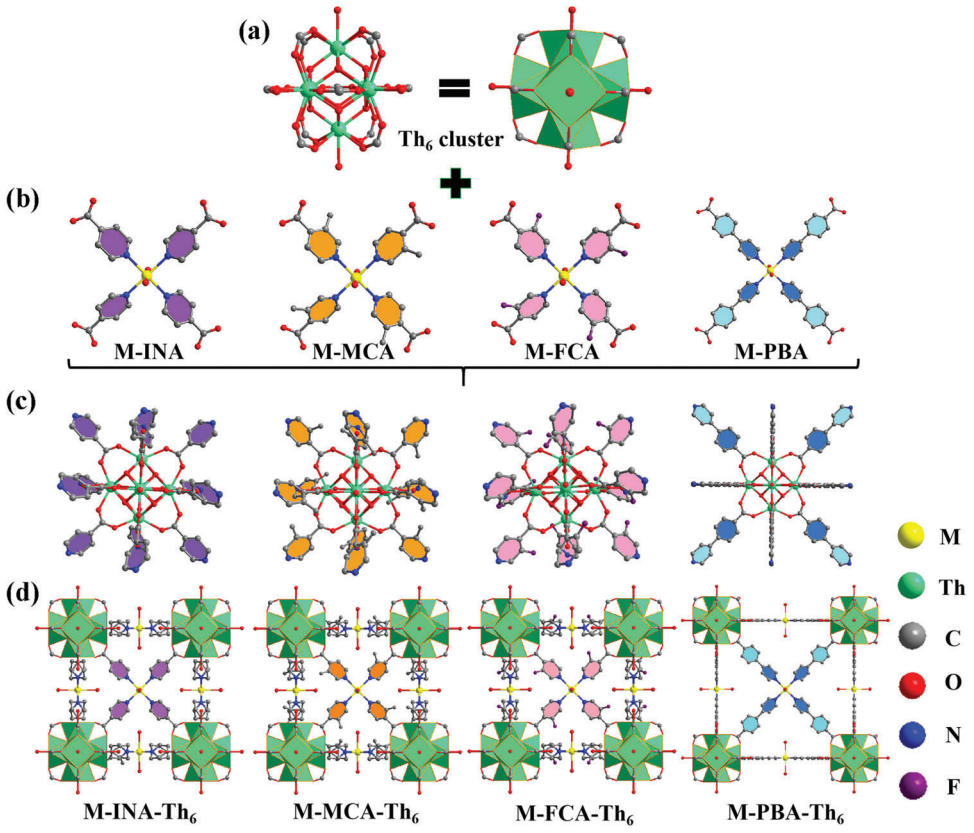

Figure 1. The crystal structures of M—Th_6—MOFs (M = Ni, Cd, and Co). a) Polyhedron model of Th_6 cluster. b) Diagram of various metal complex units. c) The coordination pattern of the Th_6 cluster in M—Ligand—Th_6. d) 3D structure of M—L—Th_6. All hydrogen atoms were omitted for clarity.

3.26, 3.53, 3.49, 3.45, 3.26, 3.27, 3.37, 3.97, 3.68, 3.99, and 3.96 eV, respectively (Figures S27–S29, Supporting Information).[20] Subsequently, the flat-band potentials of M—L—Th_6 MOFs were obtained from the *x*-axis intercepts of the linear regions in the Mott–Schottky plots (Figures S30–S32, Supporting Information). The bottom conduction band (CB) values of M—L—Th_6 MOFs were estimated to be −0.85, −1.00, −1.10, −1.10, −0.87, −0.86, −0.97, −0.75, −1.10, −0.99, −0.89, −0.97, and −0.94 V versus normal hydrogen electrode (NHE). The positive slope in these plots implied that these M—L—Th_6 MOFs have n-type semiconductor-like properties.[21] Based on the equation $E_{VB} = E_{CB} + E_g$,[22] the top of valence band (VB) values were calculated to be 2.56 V (Ni—INA—Th_6), 2.26 V (Ni—PBA—Th_6), 2.43 V (Ni—FCA—Th_6), 2.62 V (Ni—MCA—Th_6), 2.59 V (Co—INA—Th_6), 2.39 V (Co—PBA—Th_6), 2.52 V (Co—FCA—Th_6), 2.27 V (Co—MCA—Th_6), 2.98 V (Cd—INA—Th_6), 2.79 V (Cd—INA—Th_6), 2.79 V (Cd—PBA—Th_6), 3.02 V (Cd—FCA—Th_6), and 3.02 V (Cd—MCA—Th_6) (Figures S33–S35, Supporting Information). These M—L—Th_6 MOFs had appropriate levels of VB values, which allowed them to be applied to some oxidation reactions, such as the oxidation of MPS. Besides, to evaluate the photoresponsivity of these M–L–Th_6 MOFs, transient photocurrent response tests were performed. As shown in Figures S36–S38 (Supporting Information), the photocurrent density remained relatively high. Among M—PBA—Th_6 MOFs, the transient photocurrent response cycle of Ni—PBA—Th_6 under full light conditions exhibited a stronger current density. Among of Ni—L—Th_6 MOFs, the results were similar to the above. This indicated that Ni—PBA—Th_6 had a higher photoresponsivity, which provided necessary conditions for photocatalytic oxidation of MPS.

In order to explore the application of thorium-based MOFs in catalytic reactions, the model system was applied to the photocatalytic oxidation of MPS. First, solvent screening experiments were carried out over Ni—PBA—Th_6 (Table S4, Supporting Information). Among these solvents (DMF, CH_3CN, C_2H_5OH, and CH_3OH), the optimum conversion rate and product selectivity could be obtained in CH_3OH. Subsequently, the screening of oxidants was performed, as shown in Table S5 (Supporting Information). The oxidizing ability of O_2 and *tert*-butyl hydroperoxide (TBHP) was both inferior to H_2O_2, which could not satisfy both the high conversion rate and the high selectivity of a certain product. H_2O_2 was selected as the optimal oxidant for the reaction. Based on the above experiments, MPS (0.108 mmol), 30% H_2O_2 (0.5 mmol), and catalyst (20 mg) were added to methanol solvent (4 mL), and the photocatalytic reaction was carried out for 48 h. High conversion with high selectivity to obtain the product $MPSO_2$. First of all, the photocatalytic performance of M—L—Th_6 MOFs with different second metals was carried out. For M—PBA—Th_6, the results showed that this series of catalysts were able to convert MPS into both MPSO and $MPSO_2$ products, of which Ni—PBA—Th_6 exhibited the most excellent photocatalytic activity with 99% conversion rate and 97% selectivity for $MPSO_2$ (**Figure 2**a;

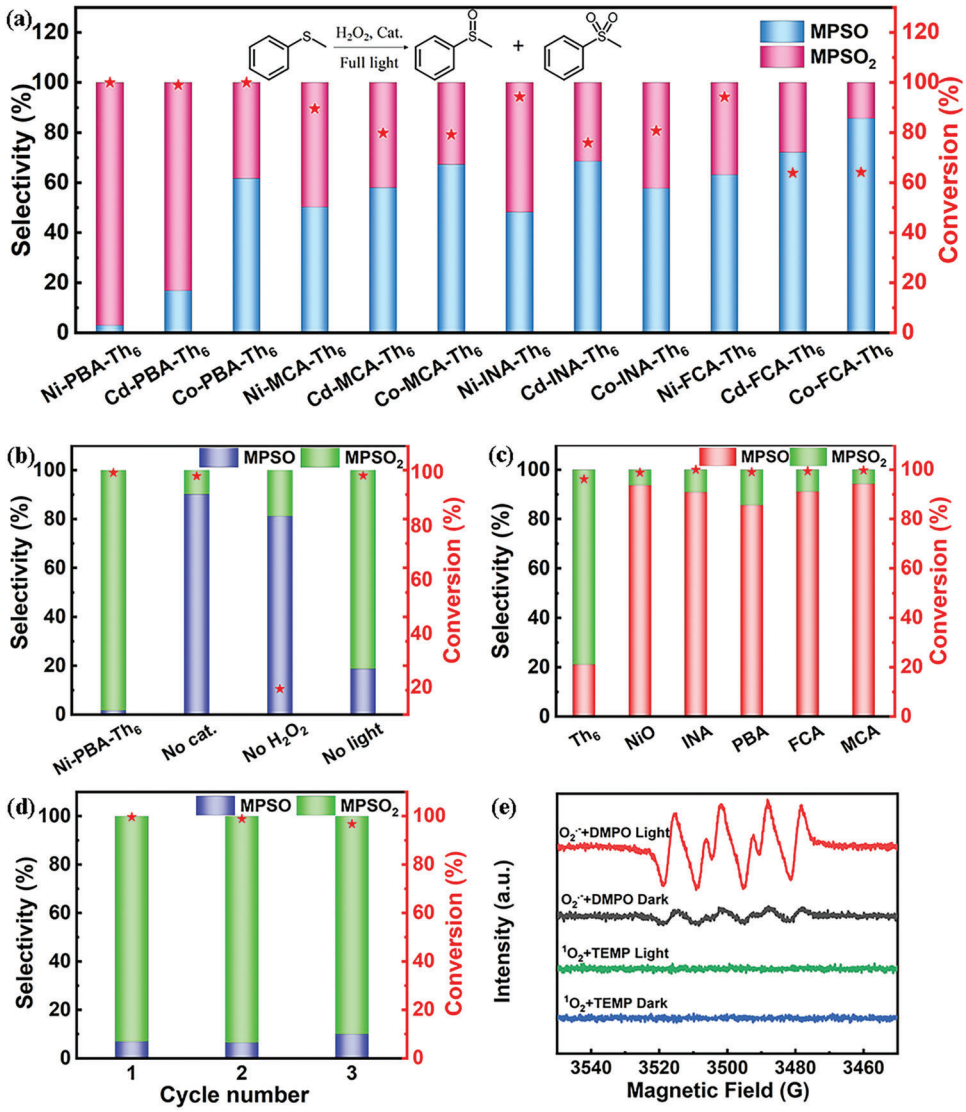

Figure 2. Photocatalytic performances of M—Th_6—MOFs. a) Conversion and selectivity of photocatalytic MPS oxidation on M—L—Th_6. b) Some comparative experiments to verify the importance of catalysts. c) Some control experiments to illustrate that the Th_6 cluster is beneficial to the oxidation of MPS to obtain the product of $MPSO_2$. d) Conversion and selectivity of catalytic oxidation of MPS with Ni—PBA—Th_6 in three repeated cycles. e) EPR spectra of Ni—PBA—Th_6 in the presence of DMPO/TEMP (a sextuplet is characteristic of DMPO-$O_2^{\cdot-}$ adducts).

Figure S39, Supporting Information). Although the conversion of Cd—PBA—Th_6 was similar to Ni—PBA—Th_6, it displayed a lower product selectivity of around 83.1% for $MPSO_2$. Compared to the above two catalysts, Co—PBA—Th_6 was much inferior. In other words, the performance sequence was Ni—PBA—Th_6 > Cd—PBA—Th_6 > Co—PBA—Th_6. For M—MCA—Th_6 (Figure S40, Supporting Information) and M—FCA—Th_6 (Figure S41, Supporting Information), the order of conversion and selectivity to $MPSO_2$ was still Ni—MCA/FCA—Th_6 > Cd—MCA/FCA—Th_6 > Co—MCA/FCA—Th_6. As for M—INA—Th_6 (Figure S42, Supporting Information), the results indicated the catalytic activity of Ni—INA—Th_6 was superior to other two catalysts. In a word, the performance of Ni modification was superior to Cd and Co in M—L—Th_6 MOFs. Divergent catalytic active centers led to variable catalytic performance, this may be due to the differences in the catalytic role of active centers and the synergy with the Th_6 cluster.

Subsequently, the photocatalytic properties of different ligands in M—L—Th_6 MOFs were evaluated. All four Co—L—Th_6 MOFs exhibited poor catalytic activities, wherein the relatively good catalyst was Co—PBA—Th_6 with a conversion rate of about 99% and a selectivity of about 38.3% for $MPSO_2$ (Figure S43, Supporting Information). Then, it was followed by Co—INA—Th_6, Co—MCA—Th_6, and Co—FCA—Th_6, with lower conversion and selectivity. The Cd—L—Th_6 MOFs exhibited better catalytic activities than Co—L—Th_6 (Figure S44, Supporting Information). Among of Cd—L—Th_6 MOFs, Cd—PBA—Th_6 showed the best catalytic performance with ≈99% conversion rate and about 83.1% selectivity for $MPSO_2$. The performance sequence was Cd—PBA—Th_6 > Cd—MCA—Th_6 > Cd—INA—Th_6 >

Cd—FCA—Th_6. Finally, Figure 2a showed that all four Ni—L—Th_6 MOFs could achieve more than 90% conversion rate in the reaction, but there were variations in the selectivity for $MPSO_2$. In these Ni—L—Th_6 MOFs, Ni—FCA—Th_6 exhibited poor selectivity for $MPSO_2$ with only 36.9%. The catalytic selectivity values of Ni—INA—Th_6 and Ni—MCA—Th_6 were similar with 51.2% and 49.7%, respectively. Ni—PBA—Th_6 achieved a high conversion rate of ≈99%, and also had a high $MPSO_2$ selectivity of ≈97%. That is, the sequence of performance was Ni—PBA—Th_6 > Ni—INA—Th_6 ≈ Ni—MCA—Th_6 > Ni—FCA—Th_6 (Table S6, Supporting Information). Even compared to the previously reported catalysts, the performance of Ni—PBA—Th_6 catalyst was excellent (Table S7, Supporting Information). To sum up, the PBA ligand was superior to the other three ligands due to the better induction and conjugation effects between phenyl and functional groups.

From the above experimental results, the overall catalytic performance of Ni—L—Th_6 MOFs was found to be superior. To explore the discrepancies in the performance of these Ni—L—Th_6 MOFs, choosing Ni—L—Th_6 as a typical model to investigate transient photocurrent patterns, transient-state photoluminescence (TSPL) spectroscopy, and carrier lifetime of these Ni—L—Th_6 MOFs (Figures S36 and S45–S49, Supporting Information). As shown in Figure S36 (Supporting Information), Ni—PBA—Th_6 exhibited the strongest photoresponsiveness, followed by Ni—INA—Th_6, Ni—MCA—Th_6, and Ni—FCA—Th_6. The results were compatible with the experimental results. Besides, Ni—PBA—Th_6 exhibited the lowest TSPL intensity and the longest carrier lifetime (τ_{av} = 0.994 ns), indicating that it displayed the highest electron–hole separation efficiency (Figures S45–S49, Supporting Information). These results verified that the functionalization of Ni—L—Th_6 MOFs by PBA ligand indeed enhanced the charge-separation efficiency and further promoted the photocatalytic oxidation reaction.

In the M—L—Th_6 system, Ni—PBA—Th_6 MOF was an excellent catalyst for the photocatalytic oxidation of MPS to $MPSO_2$ reaction. Cycle stability experiments demonstrated that Ni—PBA—Th_6 maintained good catalytic efficiency with >96% conversion rate and >90% $MPSO_2$ selectivity throughout three cycles (Figure 2d). PXRD spectra confirmed that the framework structure of Ni—PBA—Th_6 maintained its integrity after reaction (Figure S51, Supporting Information). Fourier transform infrared spectroscopy (FTIR) results indicated that its functional groups did not change after the reaction (Figure S52, Supporting Information). XPS analysis certified that the valence states of the metal elements kept consistent before and after the reaction (Figures S21–S23, Supporting Information). The above results demonstrated that Ni—PBA—Th_6 was a good heterogeneous catalyst maintaining structural integrity in the catalytic process.

Ni—PBA—Th_6 was chosen as the catalyst for the extended substrate experiments. Various thioether derivatives, including F, Cl, Br, *m*-Me, *m*-Et, *o*-Me, and propyl sulfide, were investigated in the CH_3OH–H_2O_2 system to verify the universality of the catalyst (**Figure 3**). As the results illustrated, no sulfoxide product was detected, the conversion rate of the reaction was up to 99% and the selectivity of the sulfone was about 95%. All these derivatives could be well oxidized to the corresponding sulfone.

To confirm the key factors for reaction occurrence, a range of controlled experiments were conducted (Figure 2b; Table S8, Supporting Information). Without Ni—PBA—Th_6 catalyst, the oxidation of MPS mainly accomplished the first step for MPSO generation, along with trace amounts of $MPSO_2$. The crucial experiment illustrated that the catalyst enabled efficient access to the $MPSO_2$ product. The conversion rate was only 19.6% with only 18.8% selectivity for $MPSO_2$ when without H_2O_2 in the reaction, indicating that H_2O_2 was beneficial to greatly promote the whole photocatalytic experiment. The above results also suggested that H_2O_2 played a major role in the first step (from MPS to MPSO) and catalyst played an indispensable role in the second step (from MPSO to $MPSO_2$). Furthermore, the additional experiment on photocatalytic oxidation of MPSO was performed, only trace amounts of $MPSO_2$ could be detected without Ni—PBA—Th_6 (Figure S60, Supporting Information), whereas in the presence of Ni—PBA—Th_6, the sole $MPSO_2$ product was obtained along with 93.5% conversion rate. This further illustrated the indispensable role of the catalyst in accessing the final product from MPSO to $MPSO_2$ (Table S9, Supporting Information).

Experiments were conducted under light-free conditions to investigate the role of light in the catalytic process (Table S10, Supporting Information). As shown in Figure S61 (Supporting Information), the reaction still proceeded without the light, but with significantly reduced efficiency in terms of both conversion and selectivity of $MPSO_2$. For M—PBA—Th_6 and M—MCA—Th_6, the conversion rate dropped significantly to around 8–25%, and their selectivity for $MPSO_2$ was slightly reduced by around 5–15%. As to M—INA—Th_6 along with M—FCA—Th_6, the conversion rate and selectivity were significantly decreased by 10–20%. The room-temperature catalytic performance of Ni—ligand—Th_6 also showed a significant decline in conversion rate by 10–30% and a slight loss of $MPSO_2$ product selectivity compared to photocatalysis, so that occurred for Cd—ligand—Th_6 and Co—ligand—Th_6. These results indicated that light irradiation was an essential requirement for efficiently obtaining $MPSO_2$ product, possibly due to higher efficiency in photogenerated electron and hole separation under light irradiation. In addition, control tests were carried out under light-free conditions. As shown in entries 13 and 14, poor conversion rate and selectivity were obtained in the absence of oxidant or catalyst, which revealed that catalyst and oxidant played important roles in the reaction. To ascertain the catalytic active site, we conducted several comparative tests (Figure 2c). When using nickel oxide or organic ligands as catalysts, the oxidation reaction could only proceed to the first step, leading to MPSO as the main product. However, when using the Th_6 cluster as the catalyst, it was capable of obtaining ≈96% conversion rate and ≈78% selectivity of $MPSO_2$, indicating that the catalytic center was on the Th_6 cluster for $MPSO_2$ generation.

For identifying the reactive oxygen species (ROS) involved in the reaction, electron paramagnetic resonance (EPR) experiments were conducted. In Figure 2e, the detection of all possible ROS formed by H_2O_2, such as $^1O_2$, $O_2^{\cdot-}$, and ·OH. Among them, ·OH was quenched by the methanol solvent.[23] Using 2,2,6,6-Tetramethylpiperidine-N-oxyl (TEMP) as the $^1O_2$ radical trapping agent,[24] it turned out that no signal of $^1O_2$ was detected under dark or light conditions, while adding 5,5-dimethyl-1-pyrroline-N-oxide (DMPO) as the $O_2^{\cdot-}$ radical trapping agent,[25] Ni—PBA—Th_6 under visible light irradiation showed a sixfold state signal, but a faint EPR signal could also be recognized in the dark. To verify the involvement of $O_2^{\cdot-}$ in the reaction, the

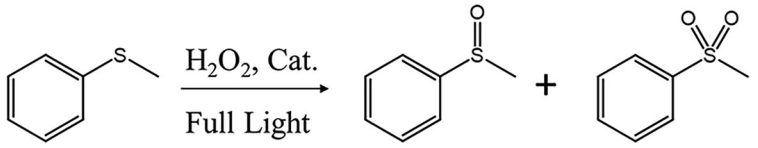

Entry	Substrate	Product	Conversion (%)	Sulfoxide selectivity (%)	Sulfone selectivity (%)
1	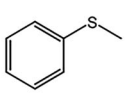	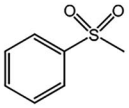	>99	2	>97
2	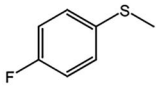	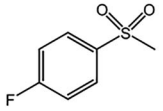	>99	-	>99
3	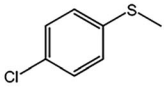	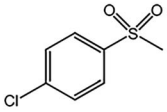	>99	-	>95
4	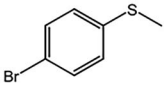	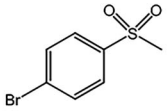	>99	-	>95
5	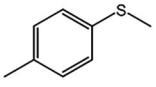	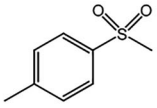	>99	-	>99
6	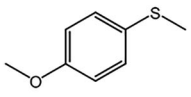	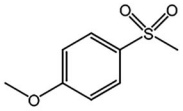	>99	-	>95
7	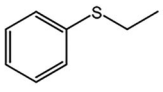	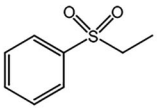	>99	-	>99
8	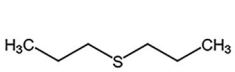	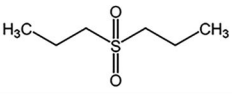	>99	-	>99

Figure 3. Photocatalytic performances of Ni—PBA—Th_6. Reaction scope on photocatalytic oxidation reaction of MPS: reaction conditions unless noted otherwise: substrate, 0.1 mmol; catalyst, 20 mg; 0.5 mmol H_2O_2 (30% w/w); solvent, 4 mL of CH_3OH; reaction time, 48 h, in full light (T = 25 °C), isolated yields.

corresponding verification experiments were performed. Adding *p*-benzoquinone to the reaction as an oxygen radical quenching agent,[26] no inhibition of the reaction was found. The catalyst still achieved over 99% conversion rate and >90% selectivity for $MPSO_2$. Thus, $O_2^{\cdot-}$ was not the key reactive oxygen in the reaction. Given these experimental outcomes, the most probable case could be that H_2O_2 participated in the photocatalytic reaction in the form of adsorbed state on the active site.

During the H_2O_2-involved MPS oxidation reaction, the results certified that the catalyst was indispensable in the highly selective oxidation of MPS to the final product ($MPSO_2$), especially reflected by that the highly selective oxidation function of the catalyst in transferring MPSO to $MPSO_2$. In order to verify the experimental results, density functional theory (DFT) analysis was carried out to further explore the catalytic mechanism of M—L—Th_6 MOFs for highly selective oxidation of MPS to

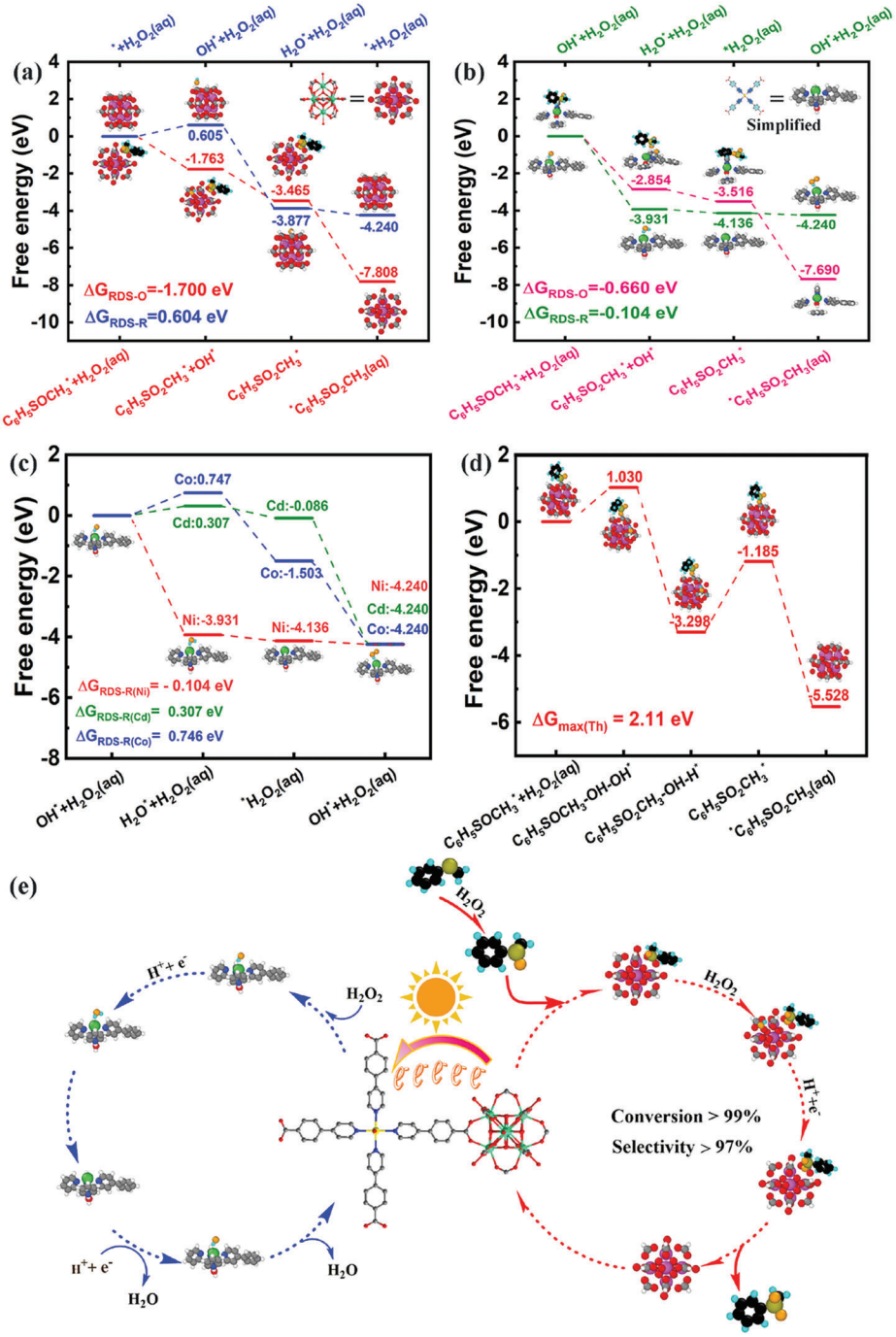

Figure 4. The DFT calculation and proposed reaction mechanism. a) Calculated Gibbs free energy distribution for the reaction of MPSO producing $MPSO_2/H_2O_2$ to produce H_2O on Th_6 cluster of Ni—PBA—Th_6. b) Calculated Gibbs free energy distribution for the reaction of MPSO producing $MPSO_2/H_2O_2$ to produce H_2O on Ni of Ni—PBA—Th_6. c) Compared the Gibbs free energy for the H_2O_2 to H_2O reaction on M of M—PBA—Th_6. d) Calculated Gibbs free energy distribution on the Th_6 cluster of Ni—PBA—Th_6 for the reaction of MPSO to produce $MPSO_2$ under light-free condition. e) Proposed reaction mechanism for the photocatalytic oxidation of MPS to $MPSO_2$ by Ni—PBA—Th_6.

$MPSO_2$. To determine the active sites, we calculated the energy barriers of catalytic sites for oxidation and reduction, respectively (**Figure 4**; Table S11, Supporting Information). After the oxidation of MPS to MPSO, the catalyst oxidized the MPSO to $MPSO_2$ in three steps subsequently. The first step was the generation of $C_6H_5SO_2CH_3^*$ and OH^* adsorbed states from the adsorbed state of $C_6H_5SOCH_3^*$ and H_2O_2 (aq) under the action of the catalytic center. In the second step, the $C_6H_5SO_2CH_3^*$ and OH^* adsorbed states obtained electrons and protons to generate the intermediate $C_6H_5SO_2CH_3^*$ adsorbed states. The third step was to

desorb/release the $C_6H_5SO_2CH_3^*$ adsorbed on the catalytic center from the catalyst. It was not difficult to find out that the energy barrier demanded in the second step (ΔG_2) was the highest, so it was the rate-determining step (RDS) during the catalysis process. For Th cluster, ΔG_{RDS} of oxidation reaction ($\Delta G_{RDS\text{-}O}$) was −1.700 eV (Figure 4a), much lower than that of Ni—PBA (−0.660 eV; Figure 4b). Moreover, the energy barrier value of the $\Delta G_{RDS\text{-}O}$ was much lower than ΔG_{RDS} of the reduction reaction ($\Delta G_{RDS\text{-}R}$). Therefore, the Th cluster was more likely to play the role of the catalytic active site for the highly selective formation of $MPSO_2$, which was also consistent with the previous experimental results. Similar to that result, the $\Delta G_{RDS\text{-}O}$ values on Cd—PBA and Co—PBA were −0.586 and −0.400 eV in Cd—PBA—Th_6 and Co—PBA—Th_6 catalysts, respectively, also much larger than the $\Delta G_{RDS\text{-}O}$ value of Th cluster (−1.700 eV) (Figures S62, S63, and S65, Supporting Information). Therefore, it could be deduced that Th cluster was still the oxidation reaction center during the catalysis. In other words, the oxidation reaction of Co—PBA—Th_6, Cd—PBA—Th_6, and Ni—PBA—Th_6 all took place on the Th cluster.

At the same time, the Gibbs free energy of the reduction reaction of H_2O_2 was calculated for different catalytic centers. As shown in Figure 4a,b, the $\Delta G_{RDS\text{-}R}$ values of the Th cluster and Ni—PBA were 0.604 and −0.104 eV, respectively, which also indicated that it was easier for the reduction reacted on Ni—PBA. In other words, Ni—PBA may be the active site for H_2O_2 reduction. Similarly, the energy barrier of the $\Delta G_{RDS\text{-}R}$ value on Cd—PBA was 0.307 eV in the reduction reaction, much smaller than that on the Th cluster (0.604 eV). Cd—PBA was the active site for H_2O_2 reduction. However, the $\Delta G_{RDS\text{-}R}$ value of the reduction reaction on Co—PBA was calculated to be 0.746 eV, higher than that on Th cluster (Figure 4c). Therefore, for the Co—PBA—Th_6 catalyst, Co—PBA could not promote the occurrence of a reduction reaction, which could be one reason to explain its lower selectivity than that of Ni—PBA—Th_6 and Cd—PBA—Th_6 catalysts. Moreover, the $\Delta G_{RDS\text{-}R}$ of reduction reaction on Ni—PBA was lower than that on Cd—PBA. Thus, the difference in $\Delta G_{RDS\text{-}R}$ values may lead to the catalytic performance decreasing in an order of Ni—PBA—Th_6 > Cd—PBA—Th_6 > Co—PBA—Th_6.

Another reason for the discrepancy in their performance could be caused by the difference in the absorption peak and electronic density of state distribution of the highest and lowest occupied molecular orbitals (HOMO and LUMO). Both Th cluster and M—PBA contributed to HOMO and LUMO (Figure S64, Supporting Information). The absorption ranged between 300 and 1000 nm. During the illuminating period, for M—PBA—Th_6 (M = Ni, Cd, and Co) crystalline molecules, photogenerated electrons transition from HOMO to LUMO, holes generated on HOMO were used for oxidation reaction, while the electrons on LUMO were utilized to promote the reduction reaction. Therefore, the flow direction of electrons involved in the effective part of the reaction was more likely to be transferred from the Th cluster to the Ni—PBA under light irradiation (Figure 4e). Figure S64 (Supporting Information) showed the variation of HOMO–LUMO electronic density information when Ni was replaced by Co and Cd. Similarly to Ni, both the Th cluster and M—PBA contributed to HOMO and LUMO in Co—PBA—Th_6 and Cd—PBA—Th_6 molecular systems. The peak of Ni—PBA—Th_6 was relatively higher and had a wider absorption except at ≈700 nm. Thus, Ni—PBA—Th_6 exhibited the best light absorption activity among the three catalysts, including the Co—PBA—Th_6 and Cd—PBA—Th_6. This might also lead to the highest selectivity of $MPSO_2$ generation on Ni—PBA—Th_6. Furthermore, the $\Delta G_{RDS\text{-}R}$ values increased in an order of Ni—PBA < Cd—PBA < Co—PBA, resulting in the different catalytic performance decreased in an order of Ni—PBA—Th_6 > Cd—PBA—Th_6 > Co—PBA—Th_6. For the slight variations in the properties of Ni—L—Th_6 (L = PBA, FCA, INA, and MCA) constructed by Ni and different ligands, Figures S64, S67, and S68 (Supporting Information) illustrated the proper reason for the diversity performance among PBA, FCA, INA, and MCA ligands, contributed by the relatively close properties in both HOMO–LUMO and absorption ranges of the four samples. Among these catalysts, Ni—PBA—Th_6 had the strongest light absorption intensity, exhibiting the highest light absorption efficiency. Coupled with the longer carrier lifetime and stronger photogenerated current, the better catalytic performance of Ni—PBA—Th_6 exhibited among the other ligands constructed Ni—L—Th_6 catalysts.

Experimental results proved that the MPS oxidation reaction could proceed under the light-free condition, but the final product could not be obtained with high conversion and high selectivity. To elucidate the catalytic mechanism, we carried out the DFT analysis of the reaction under conventional light-free conditions. We found that the $\Delta G_{max\text{-}o}$ for the oxidation reaction on the Th cluster was 2.11 eV (Figure 4d), while the $\Delta G_{max\text{-}o}$ for the same reaction on Ni was 2.67 eV in the reaction decisive step (Figure S66, Supporting Information). The energy barrier of $\Delta G_{max\text{-}o}$ for the oxidation reaction on the Th cluster was much lower than that on Ni, making the reaction more plausible to occur on the Th cluster, which is consistent with the experimental results. Under light-free conditions, both the oxidation and reduction sites on the Th cluster, and the hydrogen peroxide absorbed on the catalyst subsequently assisted to complete the whole reaction. In contrast, under the photocatalytic conditions, the oxidation site was on Th and the reduction site was on Ni; both metals synergistically catalyzed to complete the oxidation and reduction reactions, respectively. For the Th active site, the energy barrier for the oxidation reaction under the light condition (0.578 eV) was much lower than that in the absence of light (2.11 eV), rendering the reaction easier to proceed. This might be the reason of photocatalysis in obtaining sulfone product more efficiently.

Based on the experimental results and DFT calculations, the reasonable catalytic mechanism of Th_6 clusters and single-metal site in the optimal catalyst Ni—PBA—Th_6 was proposed (Figure 4e). Th_6 cluster was the catalytic site for oxidation of MPSO into $MPSO_2$, and Ni—PBA was the catalytic site for the reduction of H_2O_2. In the photocatalytic reaction, the photogenerated electrons transferred from Th_6 cluster to Ni—PBA under full spectral conditions. The differences between catalyst performances were mainly due to the divergences of electronic state density distribution on HOMO–LUMO and the distinctions of Gibbs free energy of adsorption state on active site.

3. Conclusion

In summary, we constructed a series of M—L—Th_6 MOFs, and then investigated the effect of various metal complex units

and the Th cluster on the photocatalytic oxidation of MPS to $MPSO_2$. In the H_2O_2-involved photocatalytic oxidation of $MPSO_2$, Ni—PBA—Th_6 achieved more than ≈99% conversion rate and ≈97% selectivity under full light condition, being the best-performing heterogeneous catalyst among all the M—L—Th_6 MOFs. Moreover, Ni—PBA—Th_6 exhibited excellent universality in the photocatalytic reaction. The further cross validation of experimental results and DFT calculations revealed that the Th_6 cluster acted as the active site for the for the oxidation of MPS to $MPSO_2$ and the M—ligand acted as the active site for the H_2O_2 reduction reaction. Under irradiation, photogenerated electrons flowed from Th_6 cluster to M—ligand to complete the above redox reaction.

4. Experimental Section

Preparation of Materials: All solvents and reagents were commercially available analytical grade solvents and reagents, and no further purification was required during use. $Th(NO_3)_4{\cdot}4H_2O$ and isonicotinic acid were purchased from Macklin; 4-pyridin-4-yl benzoic acid was purchased from Jinan Henghua Technology Co., Ltd.; Ni $(NO_3)_2{\cdot}6H_2O$ and nitric acid were purchased from Guangzhou chemical reagent; and 3-fluoroisonicotinic acid from Bide Pharmaceuticals, $Co(NO_3)_2{\cdot}6H_2O$, $(CH_3COO)_2Co{\cdot}4H_2O$, $(CH_3COO)_2Cd{\cdot}2H_2O$, 3-methyl-4-pyridinecarboxylic acid, methyl phenyl sulfide, and its derivatives were purchased from Aladdin.

Synthesis of M—INA—Th_6 MOFs: Caution! Th is radioactive and standard protections for radioactive materials should be followed. $Th(NO_3)_4{\cdot}4H_2O$ (0.1 mmol, 58.8 mg), $Ni(NO_3)_2{\cdot}6H_2O$ (0.1 mmol, 29.1 mg), and isonicotinic acid (0.3 mmol, 37 mg) in DMF (5 mL) were ultrasonically dissolved. The mixture was sealed in 10 mL glass vial and then heated at 85 °C for 72 h. After cooling down to room temperature, light blue cube crystals of Ni—INA—Th_6 were collected, The preparation processes of Co—INA—Th_6 and Cd—INA—Th_6 were similar to Ni—INA—Th_6 except that $Ni(NO_3)_2{\cdot}6H_2O$ (0.1 mmol, 29.1 mg) was replaced by $Co(NO_3)_2{\cdot}6H_2O$ (0.1 mmol, 29.1 mg), $(CH_3COO)_2Cd{\cdot}2H_2O$ (0.2 mmol, 53.3 mg) and nitric acid (20 µL).

Synthesis of M—PBA—Th_6 MOFs: Same as the synthesis step of M—INA—Th_6, except that isonicotinic acid was replaced with 4-pyridin-4-yl benzoic acid (1.85 mmol, 37 mg).

Synthesis of M—FCA—Th_6 MOFs: Same as the synthesis step of M—INA—Th_6, except that isonicotinic acid was replaced with 3-fluoroisonicotinic acid (2.62 mmol, 37 mg).

Synthesis of M—MCA—Th_6 MOFs: Same as the synthesis step of M—INA—Th_6, except that isonicotinic acid was replaced with 3-methyl-4-pyridinecarboxylic acid (2.70 mmol, 37 mg), and Co—MCA—Th_6 use $(CH_3COO)_2Co{\cdot}4H_2O$ (0.2 mmol, 49.8 mg) and nitric acid (20 µL) as synthetic materials.

Structural Characterization: The room-temperature PXRD measurements were recorded ranging from 1.5° to 50° on a D/max 2500 VL/PC diffractometer (Japan) with a Cu-target tube and a graphite monochromator. FTIR spectra were recorded on a Brucker Tensor 27 in the range of 4000–400 cm^{-1} using the KBr pellets. XPS was recorded using an Escalab 250Xi instrument (Thermo Scientific) equipped with an Al Kα microfocused X-ray source. UV–vis absorption spectra were acquired on a Varian Cary 5000 in the wavelength range of 200–800 nm using $BaSO_4$ as a reflectance standard. EPR experiments were conducted on Bruker EMX PLUS. The electrochemical tests were carried out with EC-Lab SP-150 workstation (Bio-Logic) and CHI660E (CH Instruments). The photocatalytic liquid products were analyzed by GC-MS (Agilent 8890 and 5977B equipped HP-5-MSUI or HP-PLOT Molesieve capillary column).

Photocatalytic Measurement: The photocatalytic oxidation of methyl phenyl sulfide activities of all the catalyst was carried out in a sealed quartz reactor at temperature of 20 °C maintained by using a thermostatic water bath. Generally, the photocatalyst (20 mg) was dispersed in 4 mL CH_3OH containing 0.1 mmol of methyl phenyl sulfide in a quartz reactor (10 mL), then 0.5 mmol 30% H_2O_2 was added, and the photoreactor was sealed. A 300 W xenon lamp (light intensity: 200 mW cm^{-2}) was used as the light source of the reaction. The reaction temperature was controlled at 298 K by cooling water circulation. After reaction, the solution was collected, centrifuged, and filtered through 0.22 µm the syringe filter to remove catalyst particles. The filtrate was identified by GC-MS, and the conversion and selectivity were analyzed by GC-MS. A similar method was used to conduct other sulfide derivatives of the same concentration, and analyzed the corresponding conversion rate by GC-MS.

The conversion of MPS and selectivity for MPSO and $MPSO_2$ product, were calculated with the following equations (Equations (1–3))

$$\text{Conversion } (\%) = \frac{C_0 - C_{MPS}}{C_0} \times 100\% \quad (1)$$

$$\text{Selectivity } (\%) \text{ of MPSO} = \frac{C_{MPSO}}{C_{MPSO} + C_{MPSO_2}} \times 100\% \quad (2)$$

$$\text{Selectivity } (\%) \text{ of } MPSO_2 = \frac{C_{MPSO_2}}{C_{MPSO} + C_{MPSO_2}} \times 100\% \quad (3)$$

where C_0 is the initial concentration of MPS; C_{MPS}, C_{MPSO}, and C_{MPSO2} stand for the concentration of the residual MPS and the corresponding product of MPSO and $MPSO_2$ at a certain time after the catalytic reaction, respectively, Selectivity is defined as selectivity relative to two products.

Supporting Information

Supporting Information is available from the Wiley Online Library or from the author.

Acknowledgements

This work was financially supported by NSFC (Grant Nos. 22225109, 22101089, 21871141, 21871142, 22071109, and 92061101); Guangdong Basic and Applied Basic Research Foundation (Grant No. 2020A1515110836); the Open Fund of Energy and Materials Chemistry Joint Laboratory of SCNU and TINCI (Grant No. SCNU-TINCI-202204).

Conflict of Interest

The authors declare no conflict of interest.

Data Availability Statement

The data that support the findings of this study are available from the corresponding author upon reasonable request.

Keywords

methyl phenyl sulfone, photocatalytic oxidation of methyl phenyl sulfide, single-metal sites, Th_6 clusters

Received: July 22, 2023
Revised: August 22, 2023
Published online:

[1] a) Z. Wang, A. T. Brown, K. Tan, Y. J. Chabal, K. J. Balkus Jr., *J. Am. Chem. Soc.* **2018**, *140*, 14735; b) N. Cooper, D. Minakata, M. Begovic, J. Crittenden, *Environ. Sci. Technol.* **2011**, *45*, 6237; c) T. Cheisson, K. D. Kersey, N. Mahieu, A. McSkimming, M. R. Gau, P. J. Carroll, E. J. Schelter, *J. Am. Chem. Soc.* **2019**, *141*, 9185.

[2] a) K. E. Knope, L. Soderholm, *Chem. Rev.* **2013**, *113*, 944; b) Y. Bai, Y. Dou, L. H. Xie, W. Rutledge, J. R. Li, H. C. Zhou, *Chem. Soc. Rev.* **2016**, *45*, 2327; c) X.-P. Wu, L. Gagliardi, D. G. Truhlar, *J. Am. Chem. Soc.* **2018**, *140*, 7904.

[3] a) Y. Li, Z. Yang, Y. Wang, Z. Bai, T. Zheng, X. Dai, S. Liu, D. Gui, W. Liu, M. Chen, L. Chen, J. Diwu, L. Zhu, R. Zhou, Z. Chai, T. E. Albrecht-Schmitt, S. Wang, *Nat. Commun.* **2017**, *8*, 1354; b) Y. Wang, W. Liu, Z. Bai, T. Zheng, M. A. Silver, Y. Li, Y. Wang, X. Wang, J. Diwu, Z. Chai, S. Wang, *Angew. Chem., Int. Ed.* **2018**, *57*, 5783; c) K. M. Ok, J. Sung, G. Hu, R. M. J. Jacobs, D. O'Hare, *J. Am. Chem. Soc.* **2008**, *130*, 3762; d) C. Falaise, J. S. Charles, C. Volkringer, T. Loiseau, *Inorg. Chem.* **2015**, *54*, 2235; e) N. P. Martin, C. Volkringer, C. Falaise, N. Henry, T. Loiseau, *Cryst. Growth Des.* **2016**, *16*, 1667.

[4] a) H. Furukawa, K. E. Cordova, M. O'Keeffe, O. M. Yaghi, *Science* **2013**, *341*, 1230444; b) M. J. Kalmutzki, N. Hanikel, O. M. Yaghi, *Sci. Adv.* **2018**, *4*, eaat9180; c) C. M. McGuirk, T. Runčevski, J. Oktawiec, A. Turkiewicz, M. K. Taylor, J. R. Long, *J. Am. Chem. Soc.* **2018**, *140*, 15924; d) X.-M. Li, Y. Wang, Y. Mu, J. Gao, L. Zeng, *J. Mater. Chem. A* **2022**, *10*, 18592.

[5] a) G. J. Deblonde, T. D. Lohrey, C. H. Booth, K. P. Carter, B. F. Parker, A. Larsen, R. Smeets, O. B. Ryan, A. S. Cuthbertson, R. J. Abergel, *Inorg. Chem.* **2018**, *57*, 14337; b) K. P. Carter, J. A. Ridenour, M. Kalaj, C. L. Cahill, *Chem. -Eur. J.* **2019**, *25*, 7114; c) Z. Gao, Y. Wang, Y. Lin, Z. Zheng, Y. Liu, Q. Jing, F. Luo, *Sci. China: Chem.* **2022**, *65*, 1544.

[6] a) X. R. Tian, Z. Y. Jiang, S. L. Hou, H. S. Hu, J. Li, B. Zhao, *Angew. Chem., Int. Ed.* **2023**, *62*, e202301764; b) H. Lu, M. Xu, Z. Zheng, Q. Liu, J. Qian, Z.-H. Zhang, M.-Y. He, Y. Qian, J.-Q. Wang, J. Lin, *Inorg. Chem.* **2021**, *60*, 18629; c) S. Hou, F. Liu, H. Xie, S. L. Hanna, K. B. Idrees, C. Zhang, X. Wang, Y. Chen, P. Li, O. K. Farha, *Inorg. Chem.* **2023**, *62*, 5479; d) S. Wang, E. V. Alekseev, J. Diwu, W. H. Casey, B. L. Phillips, W. Depmeier, T. E. Albrecht-Schmitt, *Angew. Chem., Int. Ed.* **2010**, *49*, 1057; e) Q. L. Guan, F. Xu, Y. Xiao, Z. X. You, F. Y. Bai, Y. H. Xing, *Adv. Mater. Interfaces* **2022**, *9*, 2201547; f) L. Li, T. Yu, Z. Qian, X. Wu, H. He, G. Ye, Y. Qiao, *R. Soc. Open Sci.* **2022**, *9*, 220525; g) N. Zhang, L.-X. Sun, F.-Y. Bai, Y.-H. Xing, *Inorg. Chem.* **2020**, *59*, 3964.

[7] a) L. Mei, P. Ren, Q. Y. Wu, Y. B. Ke, J. S. Geng, K. Liu, X. Q. Xing, Z. W. Huang, K. Q. Hu, Y. L. Liu, L. Y. Yuan, G. Mo, Z. H. Wu, J. K. Gibson, Z. F. Chai, W. Q. Shi, *J. Am. Chem. Soc.* **2020**, *142*, 16538; b) Z. Xu, X. Xiong, J. Xiong, R. Krishna, L. Li, Y. Fan, F. Luo, B. Chen, *Nat. Commun.* **2020**, *11*, 3163; c) L. Wang, W. Zhang, J. Ding, L. Gong, R. Krishna, Y. Ran, L. Chen, F. Luo, *Nano Res.* **2023**, *16*, 3287.

[8] a) K. Q. Hu, P. X. Qiu, L. W. Zeng, S. X. Hu, L. Mei, S. W. An, Z. W. Huang, X. H. Kong, J. H. Lan, J. P. Yu, Z. H. Zhang, Z. F. Xu, J. K. Gibson, Z. F. Chai, Y. F. Bu, W. Q. Shi, *Angew. Chem., Int. Ed.* **2020**, *59*, 20666; b) H. Xu, C. S. Cao, H. S. Hu, S. B. Wang, J. C. Liu, P. Cheng, N. Kaltsoyannis, J. Li, B. Zhao, *Angew. Chem., Int. Ed.* **2019**, *58*, 6022.

[9] a) H. Feng, X. Xiong, L. Gong, H. Zhang, Y. Xu, X. Feng, F. Luo, *Nano Res.* **2021**, *15*, 1472; b) H. Lu, J. Xie, X.-Y. Wang, Y. Wang, Z.-J. Li, K. Diefenbach, Q.-J. Pan, Y. Qian, J.-Q. Wang, S. Wang, J. Lin, *Nat. Commun.* **2021**, *12*, 2798; c) V. Stavila, A. A. Talin, M. D. Allendorf, *Chem. Soc. Rev.* **2014**, *43*, 5994.

[10] a) E. A. Dolgopolova, O. A. Ejegbavwo, C. R. Martin, M. D. Smith, W. Setyawan, S. G. Karakalos, C. H. Henager, H. C. Zur Loye, N. B. Shustova, *J. Am. Chem. Soc.* **2017**, *139*, 16852; b) K. Makarov, A. Kaushansky, M. S. Eisen, *ACS Catal.* **2021**, *12*, 273; c) O. A. Ejegbavwo, C. R. Martin, O. A. Olorunfemi, G. A. Leith, R. T. Ly, A. M. Rice, E. A. Dolgopolova, M. D. Smith, S. G. Karakalos, N. Birkner, B. A. Powell, S. Pandey, R. J. Koch, S. T. Misture, H.-C. Loye, S. R. Phillpot, K. S. Brinkman, N. B. Shustova, *J. Am. Chem. Soc.* **2019**, *141*, 11628.

[11] a) P. Li, X. Wang, K.-i. Otake, J. Lyu, S. L. Hanna, T. Islamoglu, O. K. Farha, *ACS Appl. Nano Mater.* **2019**, *2*, 2260; b) R. E. Wilson, S. Skanthakumar, G. Sigmon, P. C. Burns, L. Soderholm, *Inorg. Chem.* **2007**, *46*, 2368; c) R. D. Rogers, A. H. Bond, M. M. Witt, *Inorg. Chim. Acta* **1991**, *182*, 9; d) K. E. Knope, R. E. Wilson, M. Vasiliu, D. A. Dixon, L. Soderholm, *Inorg. Chem.* **2011**, *50*, 9696; e) K. E. Knope, M. Vasiliu, D. A. Dixon, L. Soderholm, *Inorg. Chem.* **2012**, *51*, 4239; f) C. Walther, M. Fuss, S. Büchner, *Radiochim. Acta* **2008**, *96*, 411.

[12] Q. Niu, Q. Huang, T. Y. Yu, J. Liu, J. W. Shi, L. Z. Dong, S. L. Li, Y. Q. Lan, *J. Am. Chem. Soc.* **2022**, *144*, 18586.

[13] a) G. Sipos, E. E. Drinkel, R. Dorta, *Chem. Soc. Rev.* **2015**, *44*, 3834; b) M. R. Tchalala, P. M. Bhatt, K. N. Chappanda, S. R. Tavares, K. Adil, Y. Belmabkhout, A. Shkurenko, A. Cadiau, N. Heymans, G. De Weireld, G. Maurin, K. N. Salama, M. Eddaoudi, *Nat. Commun.* **2019**, *10*, 1328.

[14] a) Y. Li, S. A. Rizvi, D. Hu, D. Sun, A. Gao, Y. Zhou, J. Li, X. Jiang, *Angew. Chem., Int. Ed.* **2019**, *58*, 13499; b) C. Dai, J. Zhang, C. Huang, Z. Lei, *Chem. Rev.* **2017**, *117*, 6929; c) W. Zhu, H. Li, X. Jiang, Y. Yan, J. Lu, J. Xia, *Energy Fuels* **2007**, *21*, 2514.

[15] a) S. Caron, R. W. Dugger, S. G. Ruggeri, J. A. Ragan, D. H. B. Ripin, *Chem. Rev.* **2006**, *106*, 2943; b) J. Wei, Z. Zhang, J. K. Tseng, I. Treufeld, X. Liu, M. H. Litt, L. Zhu, *ACS Appl. Mater. Interfaces* **2015**, *7*, 5248.

[16] a) W. M. Xu, F. F. Han, M. He, D. Y. Hu, J. He, S. Yang, B. A. Song, *J. Agric. Food Chem.* **2012**, *60*, 1036; b) M. Wang, X. Jiang, *ACS Sustainable Chem. Eng.* **2022**, *10*, 671; c) N. Wang, P. Saidhareddy, X. Jiang, *Nat. Prod. Rep.* **2020**, *37*, 246.

[17] R. Fazaeli, H. Aliyan, M. A. Ahmadi, S. Hashemian, *Catal. Commun.* **2012**, *29*, 48.

[18] a) J. Liu, W. Shi, X. Wang, *J. Am. Chem. Soc.* **2021**, *143*, 16217; b) C. Li, N. Mizuno, K. Murata, K. Ishii, T. Suenobu, K. Yamaguchi, K. Suzuki, *Green Chem.* **2020**, *22*, 3896.

[19] a) L. Jiao, H.-L. Jiang, *Chin. J. Catal.* **2023**, *45*, 1; b) J.-D. Xiao, R. Li, H.-L. Jiang, *Small Methods* **2023**, *7*, 2201258; c) K. Sun, Y. Qian, H.-L. Jiang, *Angew. Chem., Int. Ed.* **2023**, *62*, e202217565.

[20] R. López, R. Gómez, *J. Sol-Gel Sci. Technol.* **2011**, *61*, 1.

[21] H. Liu, D. Chen, Z. Wang, H. Jing, R. Zhang, *Appl. Catal., B* **2017**, *203*, 300.

[22] J. Shang, W. Hao, X. Lv, T. Wang, X. Wang, Y. Du, S. Dou, T. Xie, D. Wang, J. Wang, *ACS Catal.* **2014**, *4*, 954.

[23] a) K. M. Parker, W. A. Mitch, *Proc. Natl. Acad. Sci. USA* **2016**, *113*, 5868; b) L. Wang, B. Li, D. D. Dionysiou, B. Chen, J. Yang, J. Li, *Environ. Sci. Technol.* **2022**, *56*, 3386.

[24] L.-G. Ding, S. Wang, B.-J. Yao, W.-X. Wu, J.-L. Kan, Y. Liu, J. Wu, Y.-B. Dong, *J. Mater. Chem. A* **2022**, *10*, 3346.

[25] Q. Li, X. Lan, G. An, L. Ricardez-Sandoval, Z. Wang, G. Bai, *ACS Catal.* **2020**, *10*, 6664.

[26] X.-N. Zou, D. Zhang, T.-X. Luan, Q. Li, L. Li, P.-Z. Li, Y. Zhao, *ACS Appl. Mater. Interfaces* **2021**, *13*, 20137.